Conference Note

tag: sPH-CONF-JET-2025-XX
version: 0.1
DOI: unspecified
date: August 19, 2025

sPHENIX Conference Note

...

Measurement of dijet asymmetry in Au+Au collisions at $\sqrt{s_{\mathrm{NN}}} = 200$ GeV with the sPHENIX detector

sPHENIX Collaboration

Abstract

This sPHENIX Conference Note details the measurement of dijet asymmetry (x_J) in Au+Au collision data at $\sqrt{s_{\mathrm{NN}}} = 200$ GeV taken with the sPHENIX detector in 2024 at the Relativistic Heavy Ion Collider (RHIC). Jets are reconstructed using the anti-k_t algorithm with $R = 0.3$ from electromagnetic and hadronic calorimeter energy deposits. Events are analyzed for leading jets with $p_{\mathrm{T,1}} = 30$–43.2 GeV, and where the highest sub-leading jet with $p_{\mathrm{T,2}} > 10.1$ GeV is required to be azimuthally back-to-back ($\Delta\phi > 7\pi/8$). The pair-normalized distributions are corrected for combinatoric background, unfolded for detector effects back to the truth-particle level, and reported in different centrality intervals (0–10%, 10–30%, 30–50%, 50–90%). The x_J distributions are significantly modified in central Au+Au collisions compared to those in $p + p$ collisions, as a consequence of jet-medium interactions with the quark–gluon plasma. The results are compared to a selection of theoretical predictions.

1 Introduction

Hard scattered quarks and gluons traversing the quark-gluon plasma (QGP) have significantly modified parton showers. Their energy is shifted to larger angles away from the parton due to interactions with the medium and can also be transferred to the medium itself – see, for example, Ref. [1]. Dijet asymmetry measurements at the Large Hadron Collider (LHC) indicate substantial jet quenching in Pb+Pb collisions, utilizing $p + p$ collisions as the vacuum baseline [2, 3, 4]. Initial dijet measurements, without unfolding for detector effects to the particle level, have also been performed by the STAR experiment at the Relativistic Heavy Ion Collider (RHIC) [5]. These results have generated significant theoretical interest in understanding their origin and systematic dependence [6, 7, 8].

The sPHENIX Collaboration has measured the fully unfolded dijet asymmetry, characterized by the $x_J = p_{T,2}/p_{T,1}$ distribution, in $p + p$ collisions at $\sqrt{s} = 200$ GeV. These sPHENIX preliminary results are detailed in the sPHENIX Conference Note [9]. The analysis detailed here extends these measurements to centrality-selected Au+Au collisions at $\sqrt{s_{\mathrm{NN}}} = 200$ GeV taken with the sPHENIX detector in 2024 at RHIC.

This note presents a measurement of the dijet momentum asymmetry (x_J) distributions in Run-24 Au+Au data. Results are reported in centrality intervals of 0–10%, 10–30%, 30–50%, and 50–90%, corresponding to central, mid-central, mid-peripheral, and peripheral collisions, respectively. The analysis is performed using anti-k_{T} jets with radius parameter $R = 0.3$, and the distributions are unfolded within the kinematic selection $p_{\mathrm{T},1} = 30$–43.2 GeV and $p_{\mathrm{T},2} > 10.1$ GeV. The Run-24 $p + p$ data are also reprocessed, following the identical procedure detailed in Ref. [9], to apply the same R value and kinematic selections.

2 sPHENIX Detector

sPHENIX [10, 11] is a new detector at RHIC designed to measure jet and heavy-flavor probes of the quark-gluon plasma (QGP) created in Au+Au collisions at the Relativistic Heavy-Ion Collider (RHIC) [12]. A precision tracking system enables measurements of heavy-flavor and jet-substructure observables while the electromagnetic and hadronic calorimeter system is used for measuring the energy of jets and identifying direct photons and electrons.

Going outwards starting from the beam line, sPHENIX comprises the following subsystems [13]: the MAPS-based Vertex Detector (MVTX); the INTermediate Tracker (INTT); the Time Projection Chamber (TPC) [14]; the Time Projection Chamber Outer Tracker (TPOT) [15]; the Electromagnetic Calorimeter (EMCAL) [16, 17]; the Inner Hadronic Calorimeter (IHCAL) [17]; the 1.4 T superconducting solenoid magnet [18] and the Outer Hadronic Calorimeter (OHCAL) [17]. Except for TPOT, all detectors have full azimuthal coverage and span $|\eta| < 1.1$ in pseudorapidity. sPHENIX also includes a number of forward detectors, namely the Minimum Bias Detectors (MBD), the sPHENIX Event Plane Detectors (sEPD), and the Zero Degree Calorimeters (ZDC), that includes the Shower Maximum Detector (SMD).

sPHENIX began its commissioning process in RHIC Run-2023 with Au+Au collisions at $\sqrt{s_{\mathrm{NN}}} = 200$ GeV. During RHIC Run-2024, sPHENIX collected a large sample of transversely polarized

$p+p$ physics data at $\sqrt{s} = 200$ GeV alongside a smaller sample of Au+Au data to complete its commissioning phase in that collision system.

3 Analysis Procedure

The data used for this analysis were collected in RHIC Run 2024 Au+Au $\sqrt{s} = 200$ GeV running. Data were selected requiring the coincidence of hits in at least two tubes in each side of the MBD. Selections on the correlation of the MBD charge between both sides, and on the energies in the two ZDC sides, were applied to remove non-collision and beam backgrounds. The collision centrality was characterized by the total charge in the two MBD sides, with the trigger and offline selection requirements corresponding to $93 \pm 3\%$ of the total Au+Au inelastic cross-section [19]. The typical width of the z-vertex distribution for runs in this dataset was 15 cm. These selections yield approximately 650 million minimum-bias Au+Au events for the analysis.

Monte Carlo (MC) simulations of jet production in a Au+Au collision background were used to evaluate the performance of jet measurements and correct for detector effects on the measured jet kinematics. Pythia-8 [20] jet events were generated with the "HardQCD:all" and "PromptPhoton:all" processes for various $\hat{p}_{\mathrm{T}}^{\mathrm{min}}$ thresholds to span a large kinematic range, using the Detroit tune [21] optimized for RHIC-energy jet observables.

The Au+Au background was simulated using Hijing [22], with a flow afterburner procedure which adjusted the positions of final-state particles to match the average v_n values previously measured at RHIC as a function of centrality, p_T, and pseudorapidity [23, 24]. The Hijing simulations were generated with a z-vertex distribution similar to that in the Run-24 Au+Au data sample, and the embedded Pythia-8 event was placed at the position of the Hijing event. The combined Pythia-8 plus Hijing event was propagated through a full description of the sPHENIX detector using the Geant-4 simulation package [25] and reconstructed in a manner similar to the data. The simulation samples were reweighted in centrality and z-vertex position to match the distributions of those quantities for jet events in Au+Au data, and the jet energy resolution was adjusted to match that observed in Run-24 p+p data using the dijet bisector method [9].

Jets are reconstructed according to the anti-k_{t} algorithm [26] with $R = 0.3$ using the energy deposited in $\Delta\eta \times \Delta\phi = 0.1 \times 0.1$ calorimeter towers in the EMCal and HCals. A two-step procedure is used to estimate and subtract the underlying event (UE) in Au+Au collisions, which closely follows that outlined in Ref. [27]. In the first step, unsubtracted towers are clustered into $R = 0.2$ jets, and the subset of those jets with at least one tower above 3 GeV and a maximum-to-average tower energy ratio of $D > 3$ are used to define regions possibly consistent with jet production ("seed jets"). A ϕ-averaged UE energy density is determined in each $\Delta\eta = 0.1$ slice and in each of the three calorimeter layers, excluding towers which are within $\Delta R < 0.4$ of a seed jet from contributing. The seed jet kinematics are then updated by subtracting, tower by tower, the estimated UE energy density. In the next iteration, seed jets that have $p_{\mathrm{T}} > 7$ GeV after subtraction are used to define a new set of seeds. The UE energy density is again determined, this time excluding towers within $\Delta R < 0.4$ of the second set of seed jets. Finally, all calorimeter towers were corrected for this second estimate of the UE energy density, and jet reconstruction with $R = 0.3$ was run to determine the final subtracted jet kinematics. Importantly, the procedure used in this analyses determines a ϕ-averaged estimate of the UE energy density, and does not

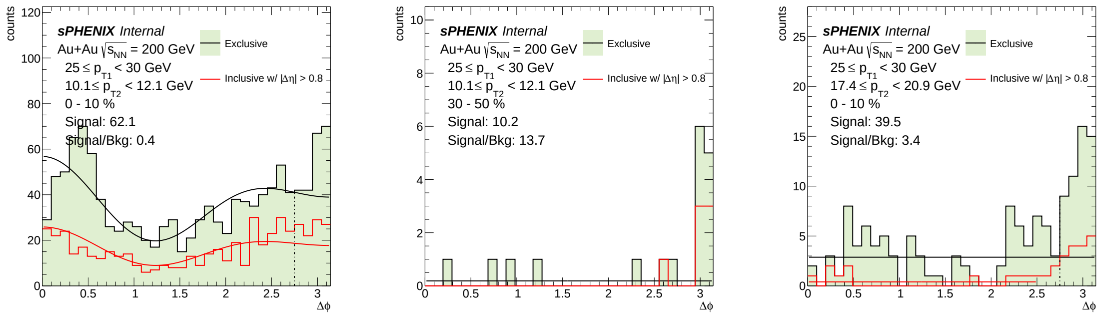

Figure 1: Examples of the combinatoric subtraction procedure for selected $p_{\mathrm{T},1} \otimes p_{\mathrm{T},2}$ ranges and centralities. Shown are the $\Delta\phi$ distributions for exclusive dijet pairs (black histogram with green fill) and inclusive pairs separated by $|\Delta\eta| > 0.8$ (red histogram). The red line shows the Fourier fit to the inclusive distribution which is used to set the $\Delta\phi$ shape, and the black line shows the estimated background in the exclusive distribution, including in the signal region $\Delta\phi > 7\pi/8$.

attempt to correct for the event-by-event hydrodynamic flow which introduces a modulation of this quantity with ϕ.

Reconstructed jets are required to be within $|\eta_{\mathrm{jet}}| < 0.8$ to ensure full containment within the calorimeter system. Events with a leading (highest-p_T) jet with $p_{\mathrm{T},1} = 30$–43.2 GeV were selected for analysis. Other jets in the event were required to have $p_{\mathrm{T},2} > 10.1$ GeV to ensure a good measurement of jet kinematics in the Au+Au UE background. The main analysis selection is an "exclusive" selection, using only the second-highest-p_T jet as the subleading jet partner to the leading jet. However, an "inclusive" selection, defined by pairing the leading jet with each of the possible additional jets in the event above 10.1 GeV, is also used in the analysis.

Dijet pairs in Au+Au events can have a significant contribution from the combinatoric pairing of a leading jet from a hard scattering with a "fake" (UE fluctuation) jet or otherwise unrelated jet, or from two such jets. This contribution is estimated in a data-driven way using sideband regions in $\Delta\phi$ and statistically subtracted from the signal yield in the region $\Delta\phi > 7\pi/8$, separately in different ranges of $p_{\mathrm{T},1} \otimes p_{\mathrm{T},2}$. The combinatoric jet contribution is expected to have a non-flat shape in $\Delta\phi$ due to influence of hydrodynamic flow. The shape of the combinatoric $\Delta\phi$ distribution is determined using an "inclusive" selection of all possible subleading jets in the given $p_{\mathrm{T},2}$ range. For this purpose, jets are required to be separated from the leading jet by $|\Delta\eta| > 0.8$, to remove the near-side contribution from other jets arising from the same hard scattering. This $\Delta\phi$ distribution is fit to a functional flow form with $v_{2,2}$ and $v_{3,3}$ components in the range $0 < \Delta\phi < 2.5$ to model the shape of the contribution from combinatoric jet pairs. This functional form is then applied to the "exclusive" $p_{\mathrm{T},1} \otimes p_{\mathrm{T},2}$ selection, where it is scaled to match the distribution in the region $0.8 < \Delta\phi < 2.5$. The integral of the function in the region $\Delta\phi > 7\pi/8$ is taken as the estimate of the combinatoric contribution to the signal, and is subtracted from the yield measured in that $p_{\mathrm{T},1} \otimes p_{\mathrm{T},2}$ selection. Fig. 1 shows an example of the procedure and the relative background contribution in different selections.

An unfolding procedure utilizing the iterative Bayesian algorithm [28] in the RooUnfold package [29] is used to correct for detector effects in the x_J measurement, including bin migration and kinematic selection inefficiency. The procedure follows closely from that used in a previous

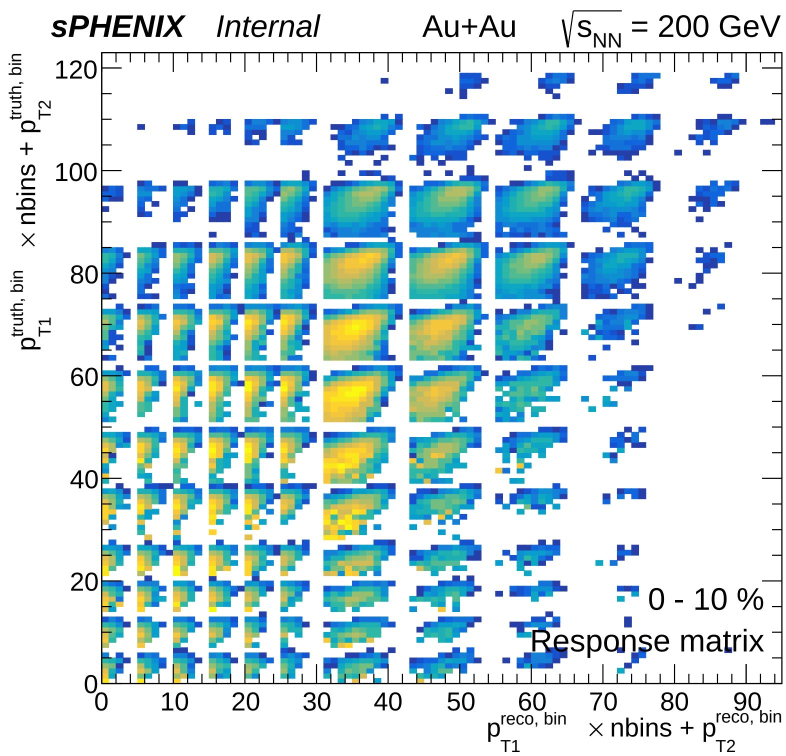

Figure 2: Response matrix for Pythia-8 jets embedded into Hijing Au+Au background, shown for 0–10% events. The x- and y-axis indices correspond to reco-level and truth-level $p_{T,1} \otimes p_{T,2}$ bins.

measurement of dijet x_J in $p + p$ collisions [9] and is summarized below. For each centrality selection, four-dimensional response matrices were populated for bin migration of the yield as a function of $p_{T,1} \otimes p_{T,2}$ from the truth to reconstructed levels, for the two highest-p_T jets that have $\Delta\phi > 7\pi/8$. An example response matrix is shown in Fig. 2. These prior distributions were reweighted by the observed $p_{T,1} \otimes p_{T,2}$ distributions at the reconstructed level in Au+Au data. The number of iterations in the unfolding procedure was chosen by optimizing the combination of the statistical uncertainty and the change in the results with respect to the previous iteration, separately for each centrality. After unfolding, the particle-level $p_{T,1} \otimes p_{T,2}$ distributions were projected to one-dimensional x_J distributions.

4 Systematic Uncertainties

The main sources of systematic uncertainty in the x_J measurement include: the jet energy scale (JES), the jet energy resolution (JER), the combinatoric subtraction, and the unfolding for detector effects. The JES and JER uncertainties includes the uncertainties in the absolute calorimeter response to p+p-like jets previously discussed in Ref. [9], as well as additional components accounting for the measurement of jets in the Au+Au dataset such as the modeling of the UE fluctuations in simulation and the potentially different response to quenched jets. The uncertainty

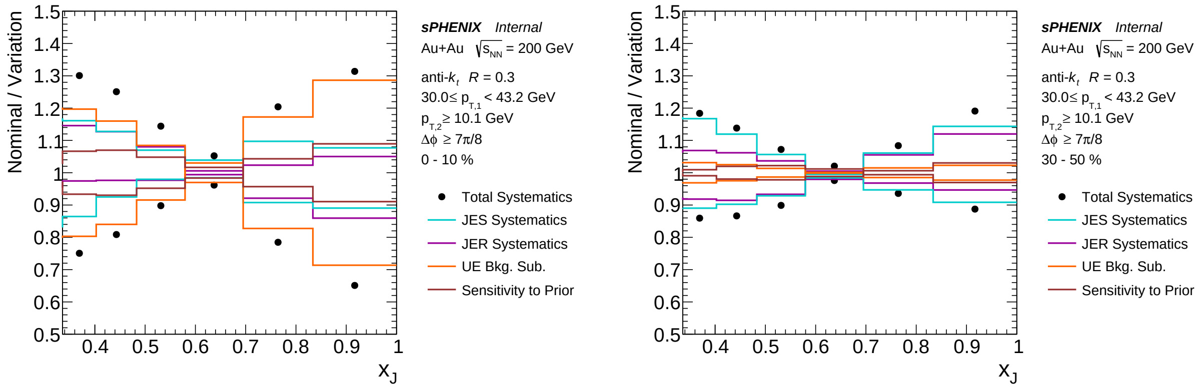

Figure 3: Summary of the magnitudes of different systematic uncertainty components and the total uncertainty for the x_J measurement in 0–10% (left) and 30–50% (right) Au+Au collisions

in the combinatoric subtraction procedure is evaluated by assuming a flat contribution in $\Delta\phi$, determined from the exclusive $\Delta\phi$ distribution, rather than a flow-modulated one. The uncertainty in the unfolding is determined by removing the significant reweighting of the prior in simulation before unfolding.

The magnitudes of individual uncertainty sources, along with the total uncertainty, are shown for two example centrality intervals in Figure 3. The dominant source of uncertainty varies depending on the centrality and the x_J region.

5 Results

The fully corrected x_J distributions are shown in Figure 4 for topologies where the leading jet lies in the range $30.0 \leq p_{T1} < 43.2$ GeV, the subleading jet satisfies $p_{T2} > 10.1$ GeV, and the azimuthal back-to-back selection $\Delta\phi > 7\pi/8$ is applied. In this selection, the subleading jet is exclusively the second-highest p_T jet in the entire event, i.e., except the leading jet, and at any η, ϕ angle. The distributions are normalized per dijet pair. The results are shown for Au+Au centrality intervals 0–10%, 10–30%, 30–50%, and 50–90%, an well as in $p+p$ collisions. In the most peripheral Au+Au events, the x_J distribution is compatible with that in $p+p$ collisions within the combined uncertainties of each measurement. However, in the other three centrality selections, the shape of the x_J distribution in Au+Au collisions is significantly modified compared to either $p+p$ or peripheral collisions, with a relative suppression at large x_J values and relative enhancement at low x_J values.

To better evaluate the centrality dependence of the data, Figure 5 shows all the Au+Au and $p+p$ data overlaid. The x_J distributions for the 0–10%, 10–30%, and 30–50% Au+Au events are compatible within uncertainties, while the 50–90% and $p+p$ distributions are significantly different. Notably, the reported observable is normalized per surviving pair, and thus the similar x_J distributions for the three most central event selections do not necessarily imply a similar level of overall jet suppression.

Figure 4 also compares the experimental results with MC event generator simulations. The data

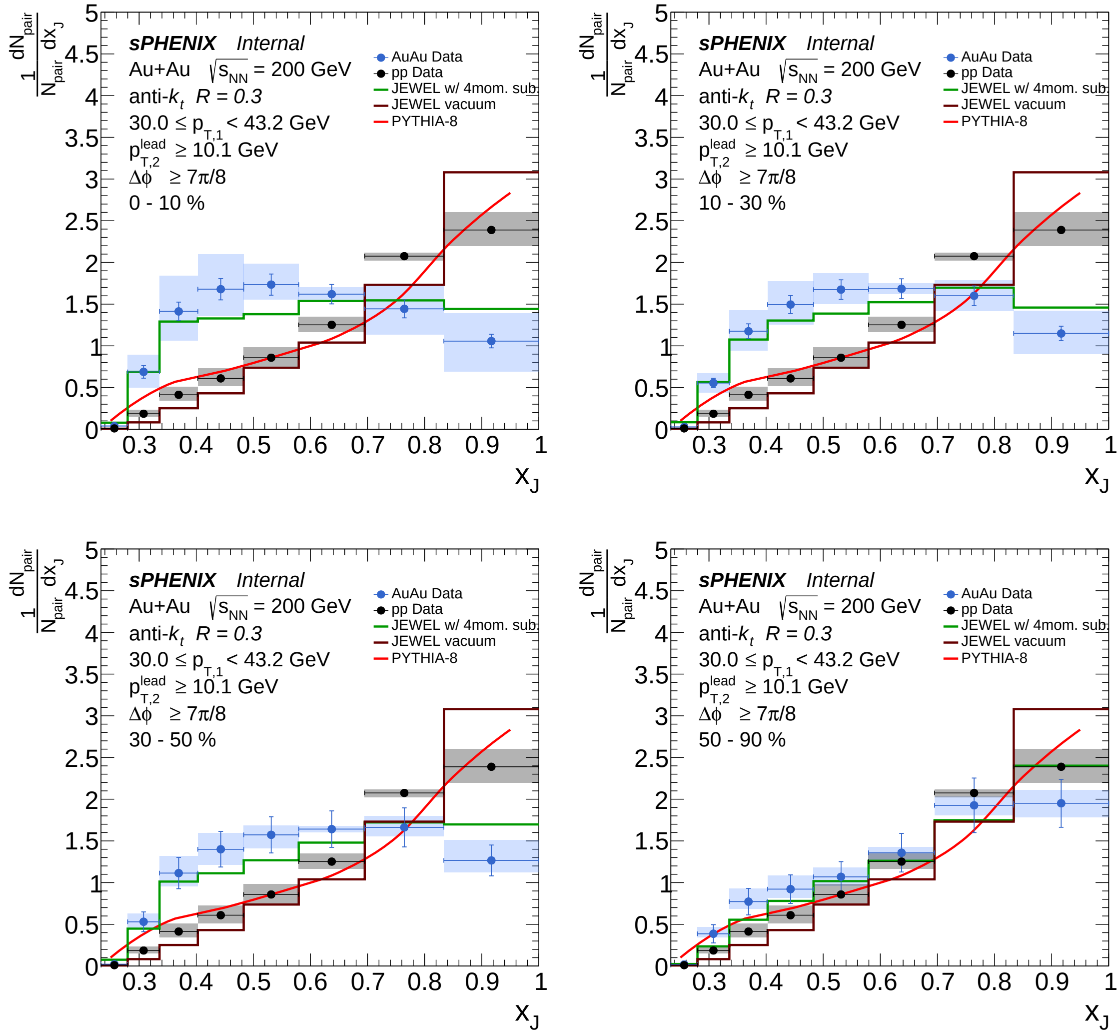

Figure 4: Fully unfolded x_J distributions of dijet events are shown (blue markers) for different Au+Au collision centrality intervals in each panel: 0–10%, 10–30%, 30–50%, and 50–90%. The x_J distributions in $p+p$ collisions are shown (black markers) with the matching kinematic selections, on each panel. For the data distributions, statistical uncertainties are shown as vertical lines and systematic uncertainties as filled boxes. Also shown are the predictions for $p+p$ collisions from Pythia-8 (red line), the Jewel Pythia-6 vacuum baseline (purple line), and Jewel medium results (green line, see text).

are compared with simulations of $p+p$ collisions from Pythia-8 using the Detroit tune [21]. These calculations agree with the sPHENIX $p+p$ data results and are close to agreement with the Au+Au peripheral 50–90% centrality interval results. In contrast, in the other three centrality intervals (30–50%, 10–30%, and 0–10%), the Au+Au data reveal significant modification relative to Pythia-8.

The data are also compared to theoretical predictions from the Jewel (Jet Evolution With Energy Loss) MC event generator, version 2.4.0, which models jet-quenching processes in QGP [30, 31]. The simulation is based on Pythia-6 and then modifies the evolution of the parton shower through

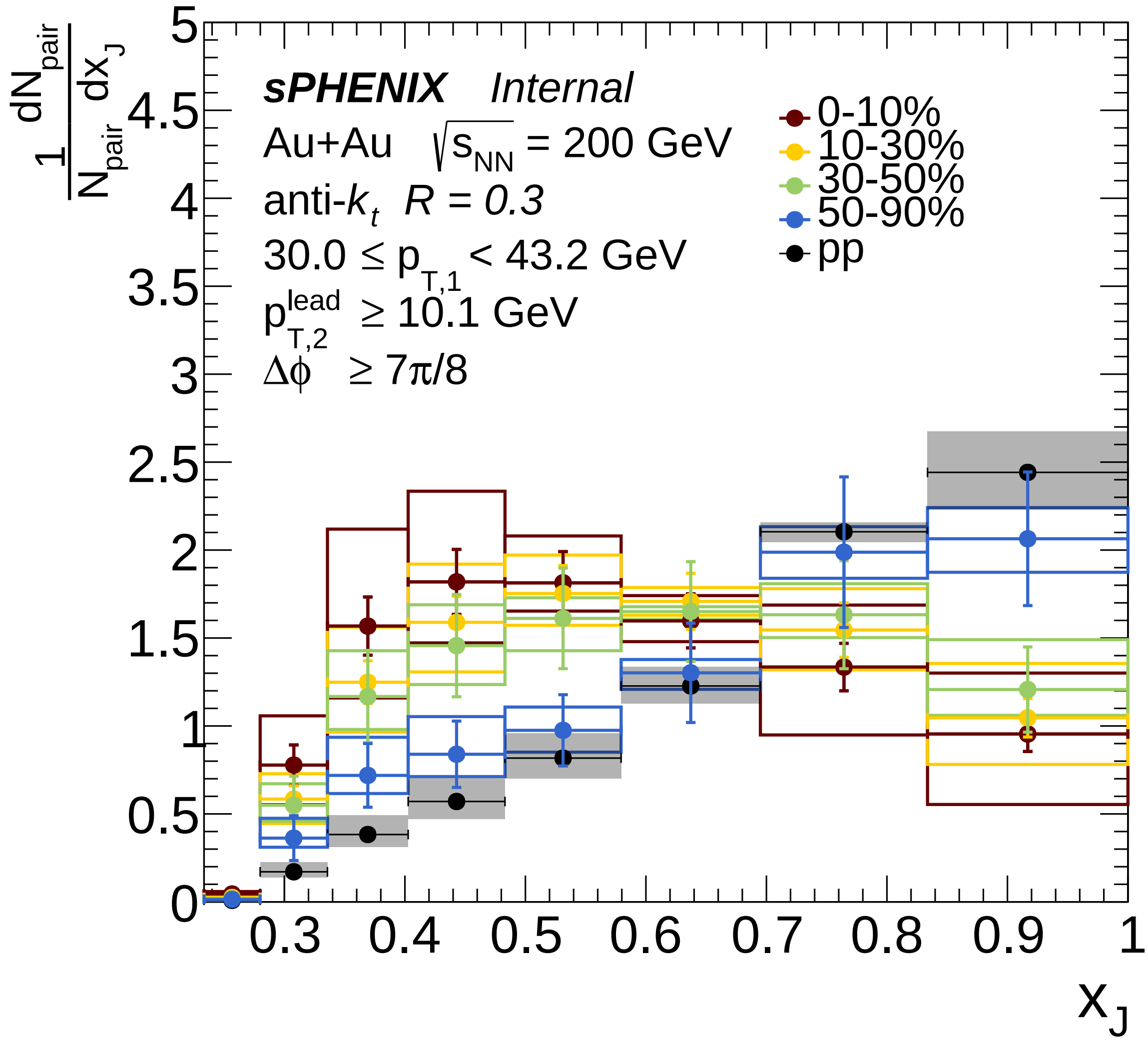

Figure 5: Fully unfolded x_J distributions of dijet events are shown for different Au+Au collision centrality intervals, 0–10%, 10–30%, 30–50%, and 50–90%, and for $p + p$ collisions with the matching kinematic selections. Statistical uncertainties are shown as vertical lines and systematic uncertainties as filled boxes.

interactions with a medium, modeled as a two-dimensional, outwardly-expanding QGP. The code was run in "vacuum" ($p + p$) mode, based on an unofficial release of Pythia-6 included with the generator, and in "simple" medium mode, modeling the 0–10%, 10–30%, 30–50%, and 50–90% Au+Au centrality intervals and matching the kinematic selections in data. The medium description used peak temperature $T_i = 375$ MeV and hydro start time $\tau_i = 0.4$ fm/c for the QGP conditions at RHIC, with other parameters set to their default values. Jets were reconstructed with the anti-k_T algorithm using $R = 0.3$ on final-state particles. For the medium output, the "4MomSub" recoil subtraction algorithm detailed in Ref. [32] was used. Figure 4 above includes a comparison of the Jewel calculation to all the Au+Au data centrality intervals. The Jewel calculation with this set of parameters reproduces the major qualitative features of the Au+Au data, including the general centrality dependence of the data.

6 Summary

This note details the measurement of dijet asymmetry (x_J) in Au+Au and $p+p$ collision data at $\sqrt{s_{NN}} = 200$ GeV, taken with the sPHENIX detector in 2024 at the Relativistic Heavy Ion Collider (RHIC). Jets are reconstructed using the anti-k_{T} algorithm with $R = 0.3$ from calorimeter energy deposits. Events that contain a leading jet with $30.0 \leq p_{T,1} < 43.2$ GeV, a subleading jet with $p_{T,2} > 10.1$ GeV, and the two jets in a back-to-back configuration, $\Delta\phi > 7\pi/8$, are analyzed. The distributions of $x_J = p_{T,2}/p_{T,1}$ are corrected for combinatoric jet pairs and detector effects, and are reported at the truth-particle level with a per-pair normalization. The x_J distributions are compared with Monte Carlo event generators Pythia-8 and Jewel. The x_J distributions in $p+p$ and peripheral Au+Au 50–90% agree within uncertainties and with Pythia-8. The more central Au+Au intervals 30–50%, 10–30%, and 0–10% reveal a substantial suppression of high-x_J jet pairs and an enhancement of low-x_J pairs compared with the $p+p$ baseline. The modifications calculated within the jet-quenching Jewel event generator, using a particular choice of medium parameters, are in qualitative agreement with the data.

References

[1] Shanshan Cao and Xin-Nian Wang. Jet quenching and medium response in high-energy heavy-ion collisions: a review. *Rept. Prog. Phys.*, 84(2):024301, 2021. arXiv:2002.04028, doi:10.1088/1361-6633/abc22b. 1

[2] Georges Aad et al. Observation of a Centrality-Dependent Dijet Asymmetry in Lead-Lead Collisions at $\sqrt{s_{NN}} = 2.77$ TeV with the ATLAS Detector at the LHC. *Phys. Rev. Lett.*, 105:252303, 2010. arXiv:1011.6182, doi:10.1103/PhysRevLett.105.252303. 1

[3] Georges Aad et al. Jet radius dependence of dijet momentum balance and suppression in Pb+Pb collisions at 5.02 TeV with the ATLAS detector. *Phys. Rev. C*, 110(5):054912, 2024. arXiv:2407.18796, doi:10.1103/PhysRevC.110.054912. 1

[4] Vardan Khachatryan et al. Measurement of transverse momentum relative to dijet systems in PbPb and pp collisions at $\sqrt{s_{\mathrm{NN}}} = 2.76$ TeV. *JHEP*, 01:006, 2016. arXiv:1509.09029, doi:10.1007/JHEP01(2016)006. 1

[5] L. Adamczyk et al. Dijet imbalance measurements in $Au+Au$ and pp collisions at $\sqrt{s_{NN}} =$ 200 GeV at STAR. *Phys. Rev. Lett.*, 119(6):062301, 2017. arXiv:1609.03878, doi:10.1103/PhysRevLett.119.062301. 1

[6] Guang-You Qin and Berndt Muller. Explanation of Di-jet asymmetry in Pb+Pb collisions at the Large Hadron Collider. *Phys. Rev. Lett.*, 106:162302, 2011. [Erratum: Phys.Rev.Lett. 108, 189904 (2012)]. arXiv:1012.5280, doi:10.1103/PhysRevLett.106.162302. 1

[7] Clint Young, Bjorn Schenke, Sangyong Jeon, and Charles Gale. Dijet asymmetry at the energies available at the CERN Large Hadron Collider. *Phys. Rev. C*, 84:024907, 2011. arXiv:1103.5769, doi:10.1103/PhysRevC.84.024907. 1

[8] José Guilherme Milhano and Korinna Christine Zapp. Origins of the di-jet asymmetry in heavy ion collisions. *Eur. Phys. J. C*, 76(5):288, 2016. arXiv:1512.08107, doi:10.1140/epjc/s10052-016-4130-9. 1

[9] sPHENIX Collaboration. Measurement of dijet imbalance (x_J) and acoplanarity ($\Delta\phi$) in p+p collisions at $\sqrt{s_{\mathrm{NN}}} = 200$ GeV with the sPHENIX detector. URL: https://www.sphenix.bnl.gov/PublicResults/sPH-CONF-JET-2025-01. 1, 3, 3, 4

[10] A. Adare et al. An Upgrade Proposal from the PHENIX Collaboration. 1 2015. arXiv:1501.06197. 2

[11] Ron Belmont et al. Predictions for the sPHENIX physics program. *Nucl. Phys. A*, 1043:122821, 2024. arXiv:2305.15491, doi:10.1016/j.nuclphysa.2024.122821. 2

[12] M. Harrison, T. Ludlam, and S. Ozaki. RHIC project overview. *Nucl. Instrum. Meth. A*, 499:235–244, 2003. doi:10.1016/S0168-9002(02)01937-X. 2

[13] The sPHENIX Collaboration. sPHENIX Technical Design Report, PD-2/3 Release, 2019. URL: https://indico.bnl.gov/event/7081/attachments/25527/38284/sphenixtdr20190513.pdf. 2

[14] Henry Klest. Overview and design of the sPHENIX TPC. *J. Phys. Conf. Ser.*, 1498:012025, 2020. arXiv:2110.02082, doi:10.1088/1742-6596/1498/1/012025. 2

[15] S. Aune et al. The sPHENIX Micromegas Outer Tracker. *Nucl. Instrum. Meth. A*, 1066:169615, 2024. arXiv:2403.13789, doi:10.1016/j.nima.2024.169615. 2

[16] C. A. Aidala et al. Design and Beam Test Results for the 2-D Projective sPHENIX Electromagnetic Calorimeter Prototype. *IEEE Trans. Nucl. Sci.*, 68(2):173–181, 2021. arXiv:2003.13685, doi:10.1109/TNS.2020.3034643. 2

[17] C. A. Aidala et al. Design and Beam Test Results for the sPHENIX Electromagnetic and Hadronic Calorimeter Prototypes. *IEEE Trans. Nucl. Sci.*, 65(12):2901–2919, 2018. arXiv:1704.01461, doi:10.1109/TNS.2018.2879047. 2

[18] T. G. O'Connor et al. Design and testing of the 1.5 T superconducting solenoid for the BaBar detector at PEP-II in SLAC. *IEEE Trans. Appl. Supercond.*, 9:847–851, 1999. doi:10.1109/77.783429. 2

[19] M. I. Abdulhamid et al. Measurement of the transverse energy density in Au+Au collisions at $\sqrt{s_{NN}} = 200$ GeV with the sPHENIX detector. 4 2025. arXiv:2504.02242. 3

[20] Torbjörn Sjöstrand, Stefan Ask, Jesper R. Christiansen, Richard Corke, Nishita Desai, Philip Ilten, Stephen Mrenna, Stefan Prestel, Christine O. Rasmussen, and Peter Z. Skands. An introduction to PYTHIA 8.2. *Comput. Phys. Commun.*, 191:159–177, 2015. arXiv:1410.3012, doi:10.1016/j.cpc.2015.01.024. 3

[21] Manny Rosales Aguilar, Zilong Chang, Raghav Kunnawalkam Elayavalli, Renee Fatemi, Yang He, Yuanjing Ji, Dmitry Kalinkin, Matthew Kelsey, Isaac Mooney, and Veronica Verkest. pythia8 underlying event tune for RHIC energies. *Phys. Rev. D*, 105(1):016011, 2022. arXiv:2110.09447, doi:10.1103/PhysRevD.105.016011. 3, 5

[22] Xin-Nian Wang and Miklos Gyulassy. HIJING: A Monte Carlo model for multiple jet production in p p, p A and A A collisions. *Phys. Rev. D*, 44:3501–3516, 1991. doi:10.1103/PhysRevD.44.3501. 3

[23] Jiangyong Jia and Soumya Mohapatra. Disentangling flow and nonflow correlations via Bayesian unfolding of the event-by-event distributions of harmonic coefficients in ultrarelativistic heavy-ion collisions. *Phys. Rev. C*, 88(1):014907, 2013. `arXiv:1304.1471`, `doi:10.1103/PhysRevC.88.014907`. 3

[24] B. B. Back et al. Centrality and pseudorapidity dependence of elliptic flow for charged hadrons in Au+Au collisions at s(NN)**(1/2) = 200-GeV. *Phys. Rev. C*, 72:051901, 2005. `arXiv:nucl-ex/0407012`, `doi:10.1103/PhysRevC.72.051901`. 3

[25] S. Agostinelli et al. GEANT4 - A Simulation Toolkit. *Nucl. Instrum. Meth. A*, 506:250–303, 2003. `doi:10.1016/S0168-9002(03)01368-8`. 3

[26] Matteo Cacciari, Gavin P. Salam, and Gregory Soyez. FastJet User Manual. *Eur. Phys. J. C*, 72:1896, 2012. `arXiv:1111.6097`, `doi:10.1140/epjc/s10052-012-1896-2`. 3

[27] J. A. Hanks et al. Method for separating jets and the underlying event in heavy ion collisions at the BNL Relativistic Heavy Ion Collider. *Phys. Rev. C*, 86:024908, 2012. `arXiv:1203.1353`, `doi:10.1103/PhysRevC.86.024908`. 3

[28] G. D'Agostini. Improved iterative Bayesian unfolding. In *Alliance Workshop on Unfolding and Data Correction*, 10 2010. `arXiv:1010.0632`. 3

[29] Tim Adye. Unfolding algorithms and tests using RooUnfold. In *PHYSTAT 2011*, pages 313–318, Geneva, 2011. CERN. `arXiv:1105.1160`, `doi:10.5170/CERN-2011-006.313`. 3

[30] Korinna Zapp, Gunnar Ingelman, Johan Rathsman, Johanna Stachel, and Urs Achim Wiedemann. A Monte Carlo Model for 'Jet Quenching'. *Eur. Phys. J. C*, 60:617–632, 2009. `arXiv:0804.3568`, `doi:10.1140/epjc/s10052-009-0941-2`. 5

[31] Korinna C. Zapp. JEWEL 2.0.0: directions for use. *Eur. Phys. J. C*, 74(2):2762, 2014. `arXiv:1311.0048`, `doi:10.1140/epjc/s10052-014-2762-1`. 5

[32] Raghav Kunnawalkam Elayavalli and Korinna Christine Zapp. Medium response in JEWEL and its impact on jet shape observables in heavy ion collisions. *JHEP*, 07:141, 2017. `arXiv:1707.01539`, `doi:10.1007/JHEP07(2017)141`. 5